Surface & Coatings Technology 206 (2012) 3186–3195

Contents lists available at SciVerse ScienceDirect

Surface & Coatings Technology

journal homepage: www.elsevier.com/locate/surfcoat

Effects of surface alloying on electrochemical corrosion behavior of oxygen-plasma-modified biomedical magnesium alloy

Guosong Wu [a], Kai Feng [a], Ali Shanaghi [a], Ying Zhao [a], Ruizhen Xu [a], Guangyin Yuan [b,*], Paul K. Chu [a,**]

[a] Department of Physics and Materials Science, City University of Hong Kong, Tat Chee Avenue, Kowloon, Hong Kong, China
[b] National Engineering Research Center of Light Alloy Net Forming, Shanghai Jiao Tong University, Shanghai 200240, China

ARTICLE INFO

Article history:
Received 19 October 2011
Accepted in revised form 2 January 2012
Available online 9 January 2012

Keywords:
Magnesium alloys
Biomaterials
Plasma immersion ion implantation
Alloying
Corrosion

ABSTRACT

Mg–3Nd–0.2Zn–0.4Zr alloy with good mechanical properties is a new type of biodegradable magnesium alloy. In order to improve the surface stability in the initial healing stage and foster tissue growth on biomedical implants made of this Mg alloy, oxygen plasma immersion ion implantation (O-PIII) is conducted to modify the alloy surface. Although O-PIII increases the thickness of the surface oxide, no significant improvement in the surface corrosion resistance is observed. Hence, surface alloying with Al and Cr by means of high-energy ion implantation is conducted prior to O-PIII. The electrochemical data obtained in simulated body fluids, including polarization curves and electrochemical impedance spectra (EIS), reveal that the surface corrosion resistance is improved after surface alloying. Our results show that surface alloying with Cr produces the best result in this study. The improvement stems from the formation of Al or Cr-containing oxide films in the implanted layer.

1. Introduction

Magnesium-based materials such as AZ91, WE43 and LAE442 are potential biodegradable materials due to their unique biodegradability and Young's moduli similar to that of human bone [1–7]. Under physiological conditions, some undesirable elements such as aluminum can be leached into body fluids and tissues and so it is important to design safe and effective magnesium-based materials to meet clinical demand. Recently, a new type of magnesium alloy, Mg–3Nd–0.2Zn–0.4Zr, has been shown to be potentially suitable due to its excellent mechanical properties and uniform corrosion in the physiological environment [8,9]. A small quantity of Nd, a rare earth element, is incorporated into magnesium alloys to increase the mechanical strength based on the strengthening principles of solid solution and precipitation, but the Nd concentration is usually low to minimize cytotoxicity [10]. Compared to Ti alloys, CoCr alloys, and stainless steels, magnesium-based biomedical materials are more reactive and the interface between the affected tissues and magnesium implants in the physiological environment is dynamic [11]. Therefore, retarding degradation during healing is crucial to proper tissue growth on the implants. The degradation rate is typically quite high in the initial stage but decreases significantly with time [12] and hence, it is critical to control the initial biodegradation rate in clinical applications.

Magnesium corrosion is affected by the thin surface oxide film and dissolution typically occurs on the oxide-free areas [13]. The native surface oxide film formed upon exposure to air consists of mainly MgO [14,15]. According to thermodynamics, MgO is not stable in an aqueous solution and will be converted into magnesium hydroxide [14,16]. If chloride ions also exist in the medium, OH^- will be substituted by Cl^- to form chloride which expedites dissolution of the surface structure [16]. Obviously, both densification and thickening of the surface oxide film will slow this process. A feasible means to improve the chemical stability of the surface oxide film is to add small amounts of specific reactive species into the metal substrate. For example, in Fe–Cr, Fe–Al, and Fe–Cr–Al alloys, addition of chromium or aluminum forms stable Cr_2O_3 or Al_2O_3 on the surface [17–20]. However, magnesium is very reactive and its affinity to oxygen is higher than that of aluminum or chromium [21,22]. Therefore, formation of protective Cr_2O_3 and Al_2O_3 may be difficult to implement in magnesium alloys under normal circumstances.

The elemental composition and temperature play important roles in the formation and growth of the surface oxide film [23]. In prior studies [24–27], yttrium and nitrogen were introduced into magnesium alloys by ion implantation and the oxidation resistance and corrosion resistance were enhanced. Ion implantation provides the possibility of introducing a wide range of different atomic species into a substrate independent of thermodynamic factors. In particular, in plasma immersion ion implantation (PIII), conformal implantation into objects with complex geometry can be achieved. If the sample is immersed in a plasma and then pulsed-biased to a high negative potential, a plasma sheath forms around the sample and ions are accelerated across the plasma heath normal to the surface [28]. Although a surface

* Corresponding author. Tel.: +86 21 3420 3051; fax: +86 21 3420 2794.
** Corresponding author. Tel.: +852 3442 7724; fax: +852 3442 0542.
E-mail addresses: gyyuan@sjtu.edu.cn (G. Yuan), paul.chu@cityu.edu.hk (P.K. Chu).

0257-8972/$ – see front matter © 2012 Elsevier B.V. All rights reserved.
doi:10.1016/j.surfcoat.2012.01.001

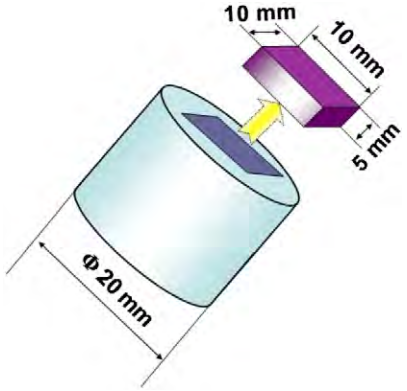

Fig. 1. Schematic presentation of the samples cut from the extruded Mg alloy rod.

Table 1
Processing parameters used in the experiment.

Process		Treatment time			
		O-3h	O-5h	Al–O	Cr–O
(I) Surface alloying	Target: Al; Base pressure: 1×10^{-4} Pa; Acceleration voltage: 35 kV; Acceleration current: 2.1 mA;			1 h	
	Target: Cr; Base pressure: 1×10^{-4} Pa; Acceleration voltage: 30 kV; Acceleration current: 2.5 mA;				25 min
(II) Oxygen PIII	Base pressure : 10^{-5} Torr; RF power: 1000 W; Pulse voltage: 20 kV; Pulse width: 50 μs; Pulse frequency: 100 Hz; Oxygen flow rate: 20 sccm;	3 h	5 h	3 h	3 h

coating can mitigate corrosion on magnesium alloys in aggressive environments including physiological media [29–33], layer delamination and interfacial mismatch can cause failure. Moreover, most coatings are non-biodegradable and inflammation can occur if they are broken and remain in the human body for a prolonged duration. Compared to coatings, ion implantation has many advantages. Coating delamination is no longer an issue and the surface properties including biocompatibility and cytotoxicity can be selectively controlled by implanting a suitable amount of the appropriate elements.

Oxygen plasma immersion ion implantation (O PIII) has been utilized to improve the corrosion resistance of AZ31 magnesium alloy [34]. In this study, we perform O-PIII to modify the surface of Mg–3Nd–0.2Zn–0.4Zr alloy and investigate the synergistic effects offered by surface alloying by means of metal (Al and Cr) ion implantation prior to O-PIII. Polarization tests and electrochemical impedance spectra [35,36] are used to investigate the electrochemical corrosion behavior of the surface modified magnesium alloy in simulated body fluids.

2. Experimental details

An extruded Mg–3.0 wt.% Nd–0.2 wt.% Zn–0.4 wt.% Zr alloy (denoted as JDBM) rod was used in this study. The samples with dimensions of 10 mm × 10 mm × 5 mm were cut from the rod as shown in Fig. 1. Prior to plasma modification, they were mechanically polished using up to 1 μm alumina paste and ultrasonically cleaned in ethanol. The process was divided into two parts, firstly surface alloying with metal ion implantation followed by oxygen plasma immersion ion implantation (PIII). Furthermore, O-PIII without metal implantation was conducted for comparison. A GPI-100 metal ion implanter in the Plasma Laboratory of City University of Hong Kong was used to conduct O-PIII and HEMII-80 ion implanter equipped with a metal cathodic arc source manufactured by Plasma Technology Ltd. was used to conduct Al and Cr metal ion implantation. The experimental procedures and important parameters are shown in Table 1.

The microstructure of the Mg–Nd–Zn–Zr alloy was examined by optical microscopy (OM) and scanning electron microscopy (SEM) in the backscattering mode. X-ray photoelectron spectroscopy (XPS) with Al K_α irradiation was used to determine the chemical states and acquire the elemental depth profiles before and after ion implantation. The sputtering rate was estimated to be about 12 nm·min^{-1} based on similar sputtering experiments conducted on a SiO_2 reference. Atomic force microscopy (AFM) was used to study the morphology of the surface film before and after ion implantation.

Simulated body fluids (SBF) [36] were prepared to evaluate the biodegradation behavior. The electrochemical experiments were carried out on a Zahner Zennium electrochemical workstation using the conventional three-electrode technique. The potential was referenced to a saturated calomel electrode (SCE) and the counter electrode was a platinum sheet. The specimen with a surface area of 10 × 10 mm^2 was exposed to the SBF solution. After 5 min of immersion in SBF, the potential was scanned from the cathodic region to the anodic region at a scanning rate of 1 mV/s at 37 °C. The electrochemical impedance spectra (EIS) were acquired to investigate the electrode/solution interface after immersion for 5 min. The data were recorded from 100 kHz to 100 MHz with a 5 mV sinusoidal perturbing signal at the open-circuit potential.

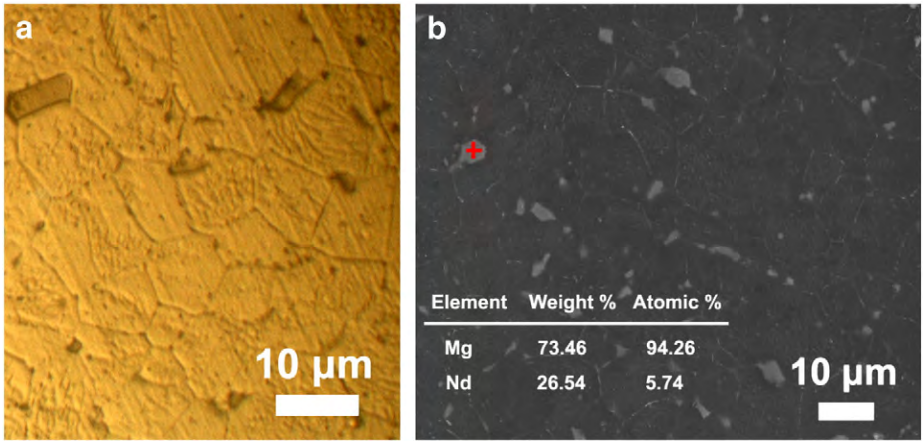

Fig. 2. Microstructure of Mg–Nd–Zn–Zr magnesium alloy observed by (a) optical microscopy and (b) back-scattered electron microscopy. The inset in (b) shows the EDS result of the non-matrix phase.

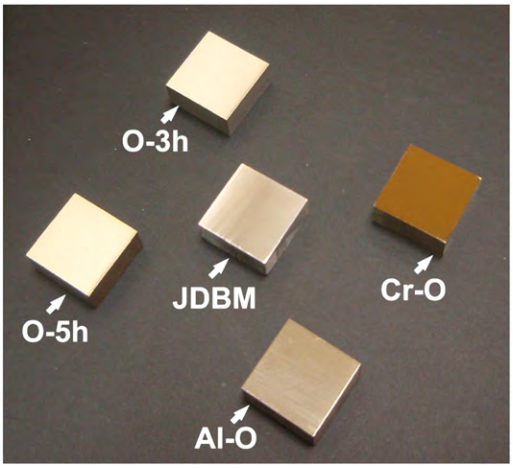

Fig. 3. Appearance of the treated and untreated samples.

3. Results and discussion

The microstructure of the Mg alloy shown in Fig. 2 reveals two phases. One is the magnesium matrix phase with fine grains and the other is the Mg_xNd_y phase. Fu et al. have confirmed the second phase as $Mg_{12}Nd$ in this Mg alloy using EDS and XRD [37]. Our EDS result shows that the atomic ratio of Mg/Nd in the second phase is about 16.4, which is close to their data considering the influence of the matrix. The sample morphology after plasma modification is displayed in Fig. 3. Surface alloying with Al in conjunction with O-PIII does not change the surface color of the Mg–Nd–Zn–Zr alloy, but Cr incorporation makes the surface dark yellow.

X-ray photoelectron spectroscopy (XPS) is used to determine the elemental depth profiles and chemical states before and after the plasma treatment. As shown in Fig. 4(a), a thin O-rich layer exists on the surface of the polished sample. With increasing sputtering time, the Mg 1s peak shifts to the left and the O peak intensity decreases gradually, showing evidence that magnesium is oxidized near the surface. Fig. 4(d) shows peak overlap with depths. According to the literature [38], the standard peak position of Nd $3d_{5/2}$ is at 980.8 eV for metallic Nd and 982 eV for Nd_2O_3. The peak overlap observed here can be attributed to the Auger peak of oxygen ($KL_{23}L_{23}$, 978 eV). The data also suggest that elemental Nd exists in the metallic state.

Figs. 5 and 6 are the XPS spectra acquired from the O-PIII Mg–Nd–Zn–Zr alloy for 3 and 5 h, respectively. The surface oxide layer is thicker after O-PIII. Because the same ion implantation energy is used in the two procedures, the oxygen penetration depth should

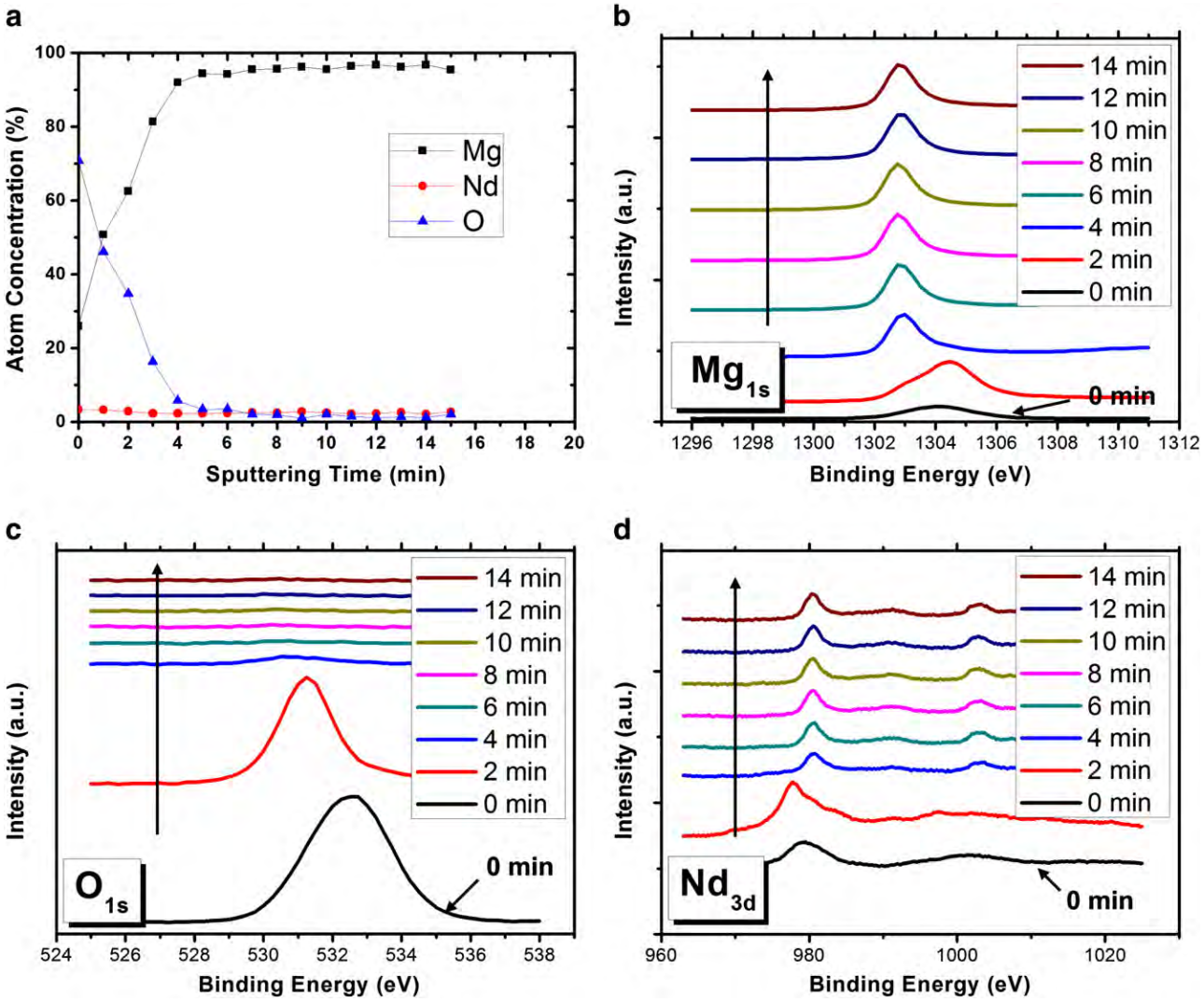

Fig. 4. XPS depth profile and high resolution XPS spectra of Mg–Nd–Zn–Zr alloy: (a) depth profile; (b) Mg_{1s}; (c) O_{1s}; (d) Nd_{3d}. The arrow shows the depth direction.

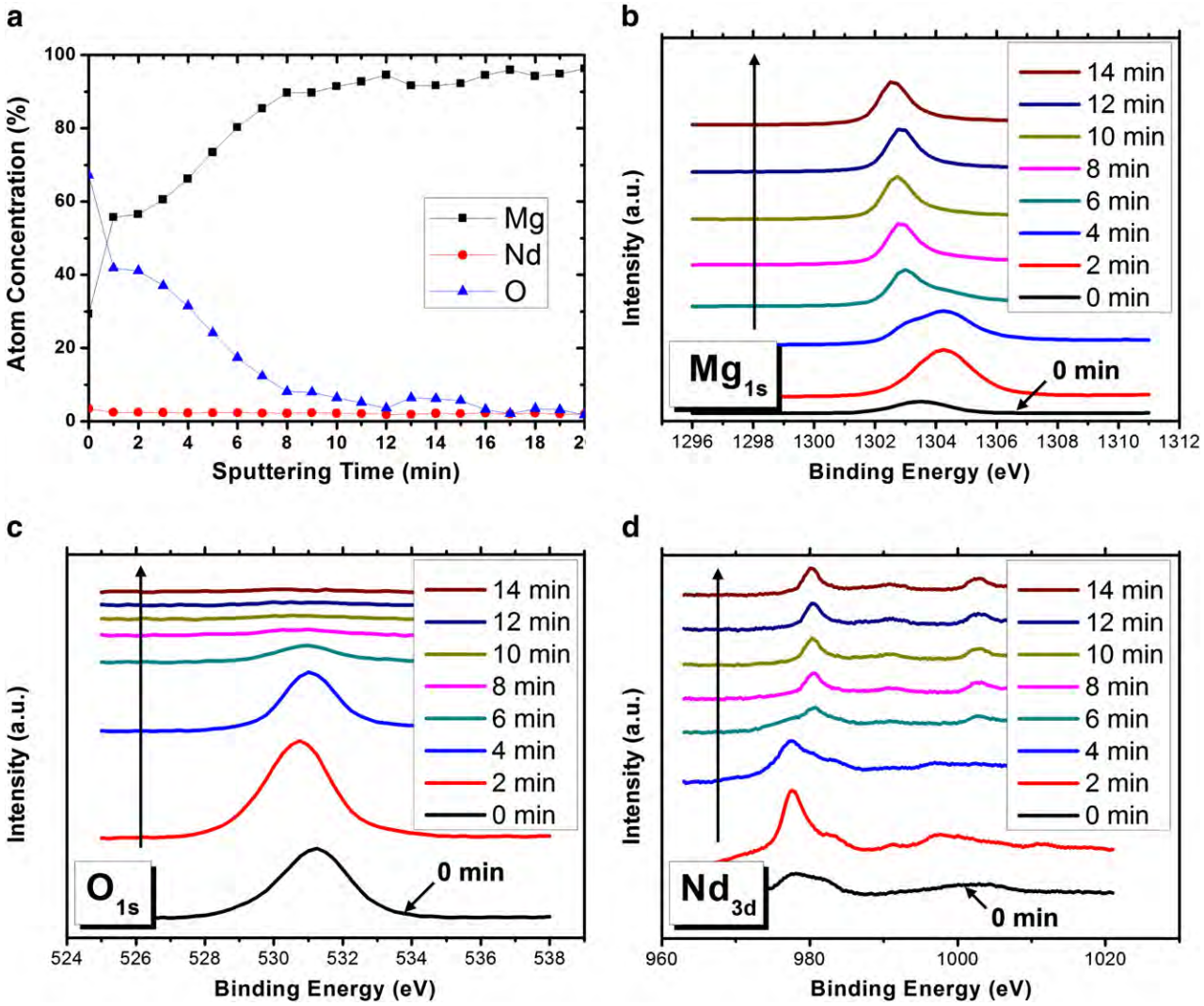

Fig. 5. XPS depth profile and high resolution XPS spectra of 3 h oxygen implanted Mg–Nd–Zn–Zr alloy: (a) depth profile; (b) Mg_{1s}; (c) O_{1s}; (d) Nd_{3d}. The arrow shows the depth direction.

be similar and O-PIII for two more hours only increases the oxygen concentration slightly due to self-sputtering. Therefore, the oxygen content in the implanted layer of the 5 h sample is close to saturation.

Figs. 7 and 8 depict the XPS spectra of the O-PIII Mg–Nd–Zn–Zr alloy with Al and Cr pre-addition, respectively. Fig. 7(a) shows a high Al peak following the surface oxygen peak in the implanted layer. According to the change of valence state shown in Fig. 7(b–e), Al exists in the oxide state in the top layer and gradually becomes metallic with depth. When the sputtering time is 2 min, Al and Mg coexist in the oxide state, suggesting that aluminum oxide is formed in the oxygen-rich region of the modified surface layer. Nd is still in the metallic state without any change in the chemical state compared to the polished and O-PIII samples. Compared to the Al and O co-implanted sample, similar phenomena can be observed from the Cr and O co-implanted sample. Owing to the different ion implantation voltages and ion species, the penetration depth of Cr is larger than that of O. When the sputtering time is 2 min, Cr exists in the oxidized state like Mg. With increasing sputtering time, Cr is gradually converted into the metallic state. In the Nd_{3d} spectra, a peak located at 997 eV emerges from the surface layer even if the Auger O peak disappears. It can be attributed to the Cr $L_{23}M_{23}M_{23}$ Auger peak.

Atomic force microscopy (AFM) is performed to examine the surface morphology of the samples. The probe is carefully scanned on the magnesium matrix in order to avoid touching the second phase. The AFM images are depicted in Fig. 9. There is no significant change between the polished and O-PIII samples. However, after aluminum or chromium surface alloying, the surface shows some random pits possibly due to ion bombardment effects from metal ion implantation.

Fig. 10 shows the polarization curves of the samples in simulated body fluids. The cathodic polarization curve is assumed to represent the cathodic hydrogen evolution through water reduction, while the anodic curve represents the dissolution of the tested metal. Generally, the corrosion potential and corrosion current density can be derived directly from the region in the cathodic polarization curves by Tafel region extrapolarization. Table 2 gives the corrosion potential and corrosion current density deduced from Fig. 10. After O-PIII, no significant shift in the corrosion potential occurs and corrosion current density is only reduced slightly. After Al or Cr surface alloying, the corrosion potential becomes higher. In particular, after Cr addition, the corrosion current density is significantly reduced compared to those of other samples in this study. The results indicate that the Cr surface alloying improves the surface corrosion resistance of the O-PIII modified Mg alloy in simulated body fluids.

Electrochemical impedance spectra (EIS) are obtained to elucidate the electrochemical reaction mechanism at the interface between the metal electrode and simulated body fluids. Fig. 11 shows the spectra

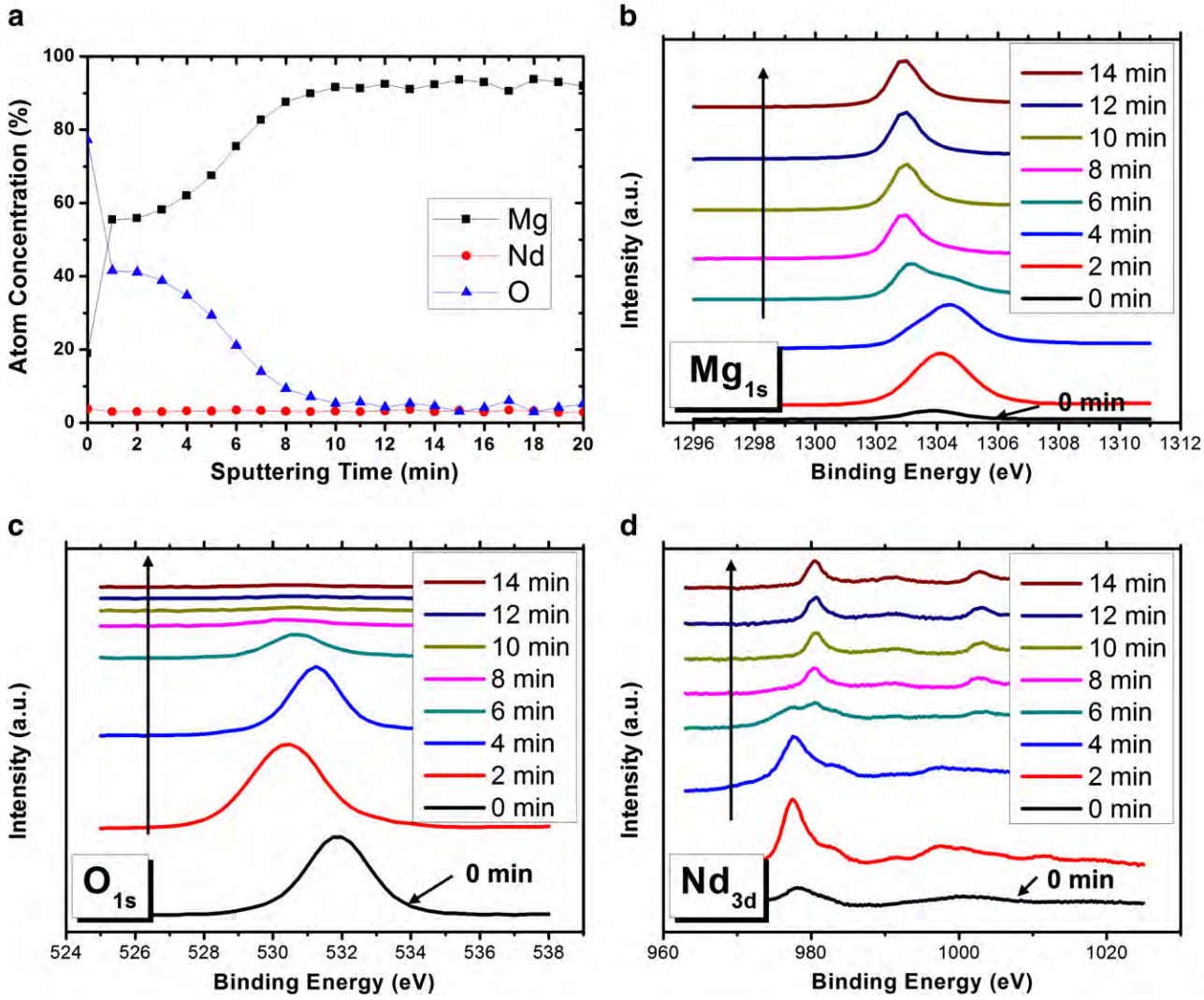

Fig. 6. XPS depth profile and high resolution XPS spectra of 5 h oxygen implanted Mg–Nd–Zn–Zr alloy: (a) depth profile; (b) Mg_{1s}; (c) O_{1s}; (d) Nd_{3d}. The arrow shows the depth direction.

of all the samples in SBF. The capacitive arc at high frequencies results from charge transfer and the capacitive arc in medium or low frequencies results from the effects of the surface film. It can be observed from Fig. 11 that the capacitive loops of the samples after surface alloying are enlarged compared to those of the O-PIII only sample. In the Al–O sample, an inductive loop is visible in the low frequency region. The low frequency region in EIS conveys important information about the electrode controlled process together with the contribution from localized defects to the overall impedance. The inductive loop is possibly associated with the formation, adsorption, and desorption of corrosion products on the surface [39–42].

According to the physical structure of the electrode, two equivalent circuit models outlined in Fig. 11 are used to fit the measured data. Model A is employed to fit the curves with two time constants, i.e. JDBM, O-3h, O-5h and Cr–O and Model B is used to fit the curve of Al–O with three time constants. Here, R_s is the solution resistance between the reference electrode and working electrode. A constant phase element, CPE_f, represents the capacitance of the surface film and R_f is the relevant resistance of the surface film. Another constant phase element, CPE_{dl}, represents the capacitance of the double layer and R_t is the charge transfer resistance related to the electrochemical reaction. In addition, L denotes the inductance and R_L represents the corresponding resistance.

Based on the two equivalent models, the data have good correlation with the experimental data and the fitted values for the individual electrical component are shown in Table 3. R_s corresponds to the solution resistance, and so the value is low and similar in all the treatments. R_t and R_f are two important parameters to evaluate the corrosion resistance and Fig. 12 presents them for comparison. For the O-PIII samples (O-3h and O-5h), both R_t and R_f are slightly improved compared to the control without plasma treatment. After surface alloying with Al and Cr, significant improvement is observed from both R_t and R_f. A higher R_t means higher resistance to magnesium dissolution and a higher R_f translates to higher resistance to mass transportation. Here, higher values of R_t and R_f also correspond to lower C_{dl} and C_f, respectively. The EIS results also indicate that surface alloying improves the surface corrosion resistance of the O-PIII magnesium alloy.

According to the polarization and EIS results, the protective effect rendered by the top surface film on the Mg–Nd–Zn–Zr alloy is not significant albeit after O-PIII which gives rise to thicker surface layers. Based on the model used in the EIS result simulation, it can be understood that the weak regions in the surface film prefer transverse propagation to longitudinal penetration in SBF. It means that the surface film consisting of mainly magnesium oxide is not stable and robust as expected. After additional surface alloying, the electrochemical

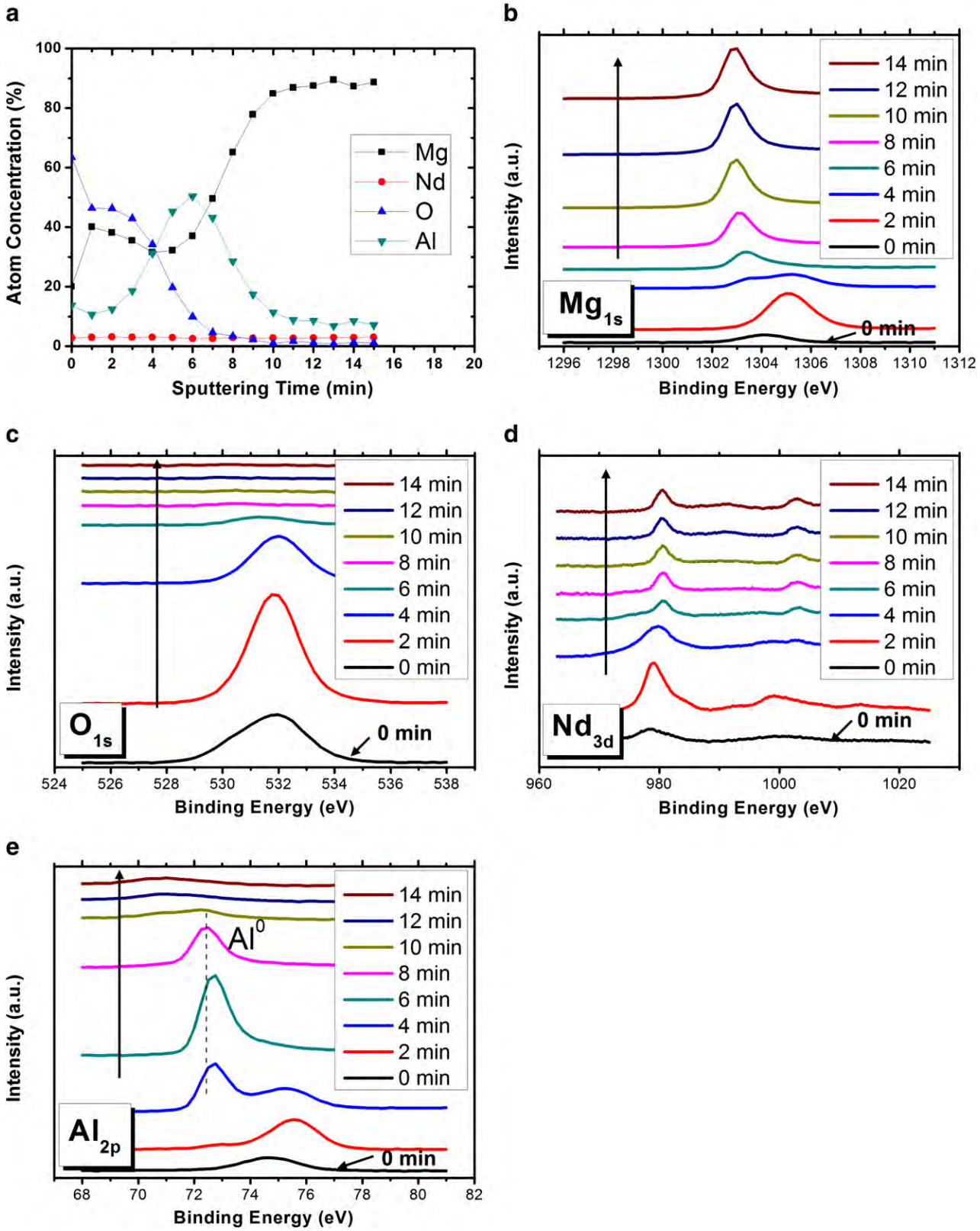

Fig. 7. XPS depth profile and high resolution XPS spectra of aluminum and oxygen implanted Mg–Nd–Zn–Zr alloy: (a) depth profile; (b) Mg_{1s}; (c) O_{1s}; (d) Nd_{3d}; (e) Al_{2p}. The arrow shows the depth direction.

corrosion behavior is obviously changed as indicated by the decreased corrosion current density and increased charge-transfer resistance. Usually, magnesium oxide is more easily formed on magnesium alloys than most other metal oxides [23]. In our process, the surface composition is altered by metal ion implantation and O-PIII replaces traditional oxidation techniques. Oxygen ions with high energy penetrate

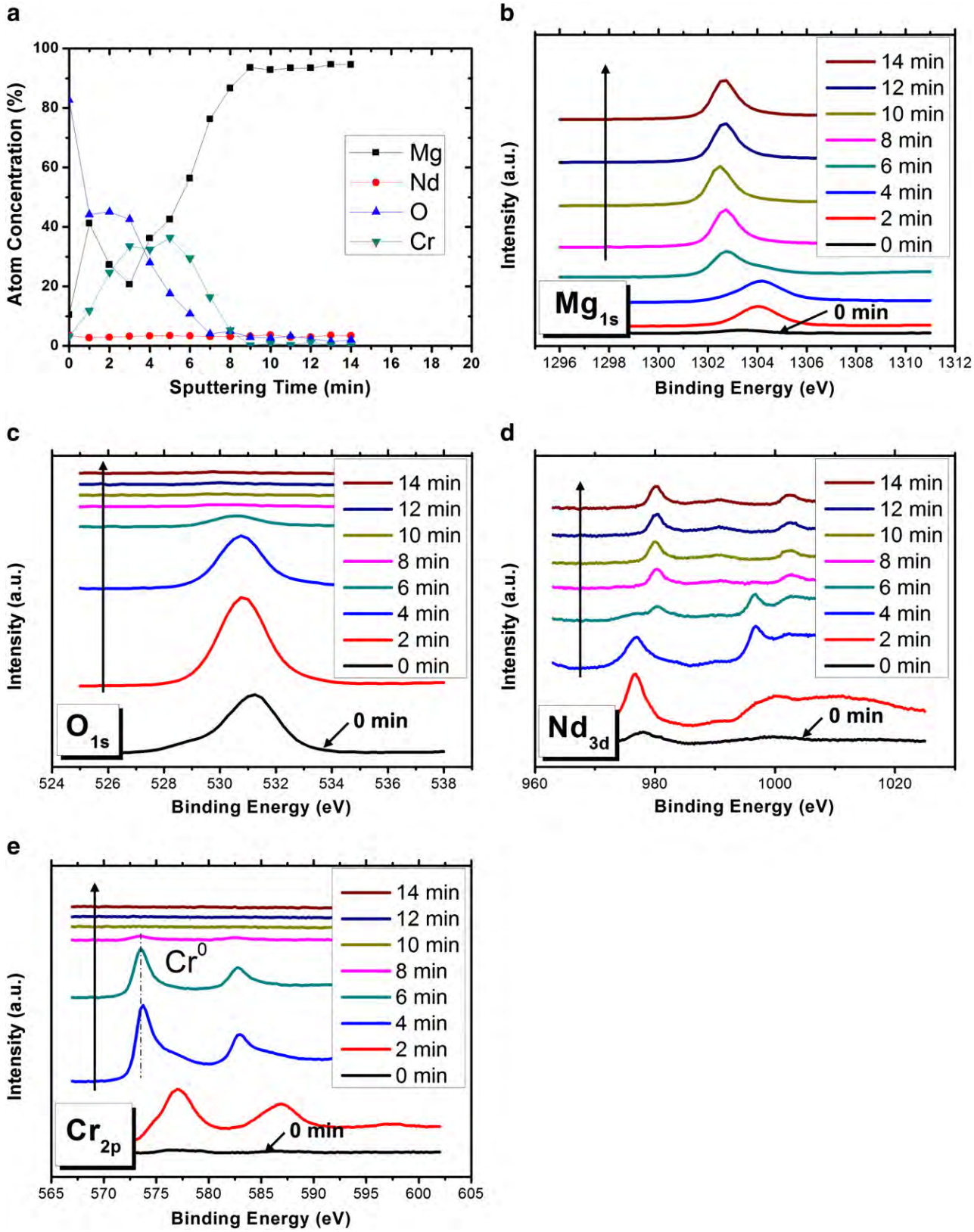

Fig. 8. XPS depth profile and high resolution XPS spectra of chromium and oxygen implanted Mg–Nd–Zn–Zr alloy: (a) depth profile; (b) Mg_{1s}; (c) O_{1s}; (d) Nd_{3d}; (e) Cr_{2p}. The arrow shows the depth direction.

the surface and react with Mg and Cr (or Al) atoms simultaneously. Because of the existence of Cr (or Al) in the modified layer, diffusion of Mg atom from the substrate to the surface is impeded and metallic Mg in the top surface will be finally depleted in the oxidation process. Therefore, it provides the chance for Cr (or Al) to co-exist with Mg in the oxidized state in the top surface. Obviously, this surface oxide

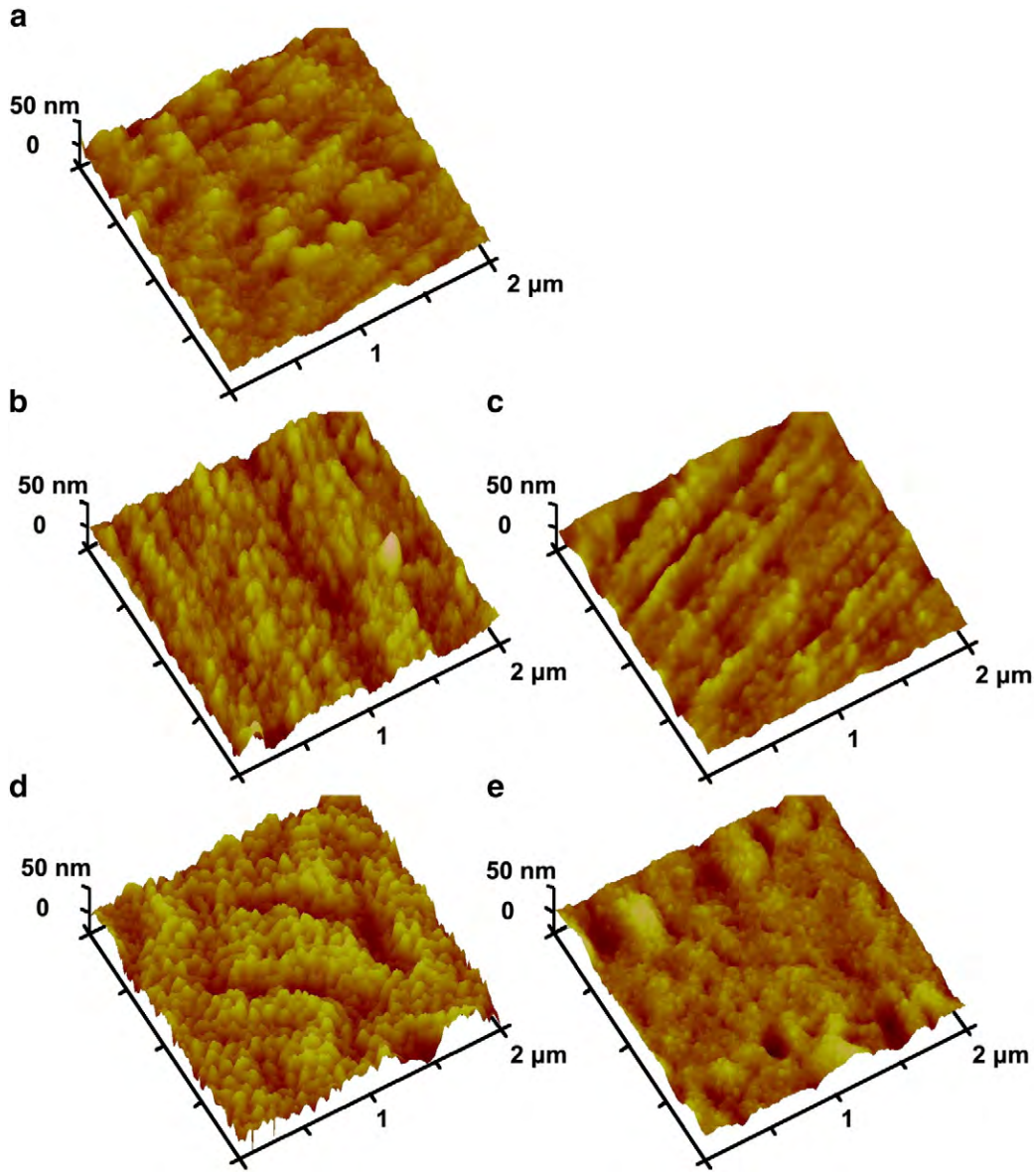

Fig. 9. AFM images of the treated samples: (a) JDBM, (b) O-3h, (c) O-5h, (d) Al–O, (e) Cr–O.

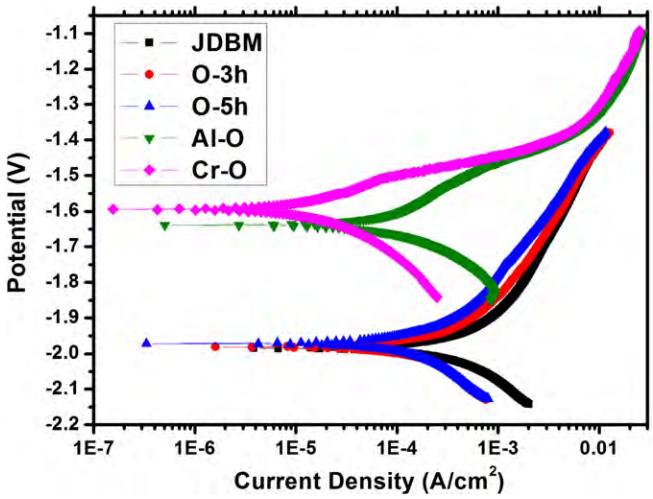

Fig. 10. Polarization curves of the treated and untreated samples in SBF.

film is more stable in SBF than those on the untreated and O-treated sample according to our electrochemical tests. The retardation effect of Al addition is much weaker compared to Cr addition. AFM reveals deep pits on the surface of the Al–O sample. An inductive loop is also present in the low frequency region in the EIS of the Al–O sample corresponding to the localized effects in the corrosion process. Therefore, it is the possible factor to reduce the improvement of its protective effect.

Table 2
Corrosion potential and corrosion current density obtained from the polarization curves.

	Corrosion potential (V)	Corrosion current density (A/cm^2)
JDBM	−1.987	4.341×10^{-4}
O-3h	−1.984	1.834×10^{-4}
O-5h	−1.973	1.671×10^{-4}
Al–O	−1.637	1.527×10^{-4}
Cr–O	−1.592	3.832×10^{-5}

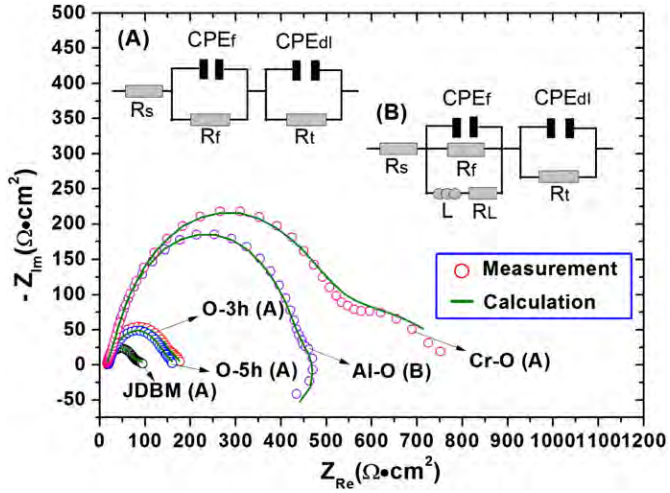

Fig. 11. Electrochemical impedance spectra (EIS) of the samples in SBF. The two inserted equivalent circuit models are used to fit the corresponding curves.

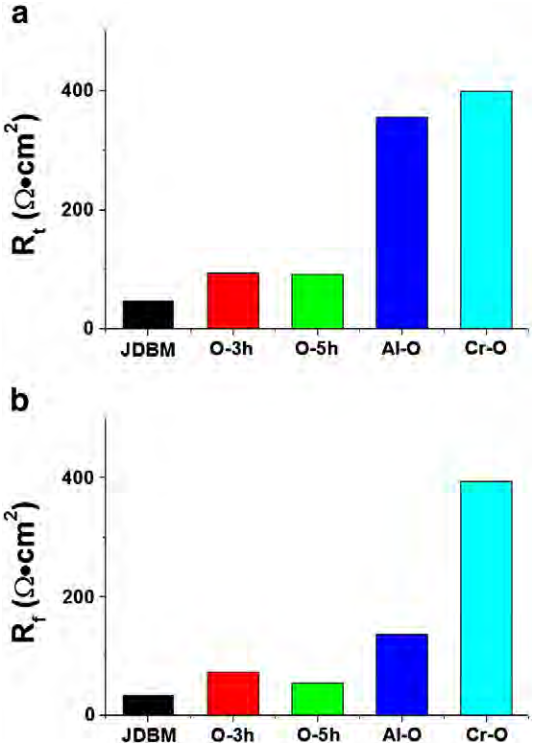

Fig. 12. Fitted data of the charge transfer resistance (R_t) and surface film resistance (R_f) in the electrochemical impedance spectra.

4. Conclusion

Although oxygen plasma immersion ion implantation increases the surface oxide thickness on biomedical Mg–3Nd–0.2Zn–0.4Zr alloy, no significant improvement in the corrosion resistance can be achieved. Surface alloying with Al or Cr can improve the performance of the O-PIII samples. Owing to the formation of Al-rich or Cr-rich oxide film on the magnesium alloy, the electrochemical behavior in simulated body fluids is changed significantly compared to samples without surface alloying. The corrosion current density decreases and the charge-transfer resistance increases after surface alloying. Our results demonstrate that surface alloying in conjunction with O-PIII is a promising approach to modify the electrochemical corrosion behavior of Mg in a physiological environment.

Acknowledgments

This work was financially supported by Hong Kong Research Grants Council (RGC) General Research Funds (GRF) No. CityU 112510 and the National Nature Science Foundation of China No. 51174136. The authors would like to thank Mr. Li Gong (Instrumental Analysis & Research Center, Sun Yat-sen University) for assistance in the XPS analysis.

References

[1] F. Witte, N. Hort, C. Vogt, S. Cohen, K.U. Kainer, R. Willumeit, F. Feyerabend, Curr. Opin. Solid State Mater. Sci. 12 (2008) 63.
[2] B. Zberg, P.J. Uggowitzer, J.F. Löffler, Nat. Mater. 8 (2009) 887.
[3] X. Gu, Y. Zheng, Y. Cheng, S. Zhong, T. Xi, Biomaterials 30 (2009) 484.
[4] X. Gu, Y. Zheng, S. Zhong, T. Xi, J. Wang, W. Wang, Biomaterials 31 (2010) 1093.
[5] E. Zhang, L. Xu, K. Yang, Scr. Mater. 53 (2005) 523.
[6] H.M. Wong, W.K. Yeung, K.O. Lam, V. Tam, P.K. Chu, D.K. Luk, M.C. Cheung, Biomaterials 31 (2010) 2084.
[7] F. Witte, V. Kaese, H. Haferkamp, E. Switzer, A. Meyer-Lindenberg, C.J. Wirth, H. Windhagen, Biomaterials 26 (2005) 3557.
[8] J. Zhang, Y. Zong, G. Yuan, J. Chang, P. Fu, W. Ding, Chin. J. Nonferr. Met. 20 (2010) 1989.
[9] X. Zhang, G. Yuan, L. Mao, J. Niu, P. Fu, W. Ding, J. Mech. Behav. Biomed. Mater. (2012), doi:10.1016/j.jmbbm.2011.05.026.
[10] X. Zhang, G. Yuan, L. Mao, J. Niu, W. Ding, Mater. Lett. 66 (2012) 209.
[11] R. Xu, G. Wu, X. Yang, T. Hu, Q. Lu, P.K. Chu, Mater. Lett. 65 (2011) 2171.
[12] Y. Xin, C. Liu, X. Zhang, G. Tang, X. Tian, P.K. Chu, J. Mater. Res. 22 (2007) 2004.
[13] G. Galicia, N. Pebere, B. Tribollet, V. Vivier, Corros. Sci. 51 (2009) 1789.
[14] G. Wu, X. Zeng, G. Yuan, Mater. Lett. 62 (2008) 4325.
[15] X. Wang, X. Zeng, G. Wu, S. Yao, Y. Lai, J. Alloys Compd. 437 (2007) 87.
[16] L. Chang, F. Cao, J. Cai, W. Liu, J. Zhang, C. Cao, Electrochem. Commun. 11 (2009) 2245.
[17] R. Wang, M.J. Straszheim, R.A. Rapp, Oxid. Met. 21 (1984) 71.
[18] I.K. Koshelev, A.P. Paulikas, M. Beno, G. Jennings, J. Linton, M. Grimsditch, S. Uran, B.W. Veal, Oxid. Met. 68 (2007) 37.
[19] Y. Kitajima, S. Hayashi, T. Nishimoto, T. Narita, S. Ukai, Oxid. Met. 73 (2010) 375.
[20] H. Buscail, S. Heinze, P. Dufour, J.P. Larpin, Oxid. Met. 47 (1997) 445.
[21] F. Noli, P. Misaelides, G. Giorginis, H. Baumann, Oxid. Met. 48 (1997) 225.
[22] I.M. Ritchie, J.V. Sanders, P.L. Weickhardt, Oxid. Met. 3 (1971) 91.
[23] X.Q. Zeng, Q.D. Wang, Y.Z. Lu, W.J. Ding, Scr. Mater. 43 (2000) 403.
[24] X. Wang, X. Zeng, G. Wu, S. Yao, Mater. Lett. 61 (2007) 968.
[25] X. Wang, X. Zeng, G. Wu, S. Yao, Appl. Surf. Sci. 253 (2006) 2437.
[26] X. Wang, X. Zeng, G. Wu, S. Yao, Y. Lai, Appl. Surf. Sci. 253 (2007) 3574.
[27] G. Wu, K. Ding, X. Zeng, X. Wang, S. Yao, Scr. Mater. 61 (2009) 269.
[28] X. Liu, P.K. Chu, C. Ding, Mater. Sci. Eng. R 47 (2004) 49.
[29] G. Song, Corros. Sci. 49 (2007) 1696.

Table 3
Fitted data of the electrochemical impedance spectra in SBF based on the corresponding equivalent circuit model.

Sample	R_s (Ω cm^2)	$Y0_{dl}$ ($10^{-5}\Omega^{-2}$ cm^{-2} s^{-n})	n_{dl}	R_t (Ω cm^2)	$Y0_f$ ($10^{-4}\Omega^{-2}$ cm^{-2} s^{-n})	n_f	R_f (Ω cm^2)	L (H cm^2)	R_L (Ω cm^2)
JDBM	17	2.979	0.9052	47.59	53.3	0.4534	34.72	0	0
O-3h	15.81	2.297	0.9379	92.94	11.3	0.5164	72.4	0	0
O-5h	18.93	2.851	0.9117	92.21	19.7	0.4811	54.46	0	0
Al–O	11.52	3.544	0.9702	354.9	14	0.3497	135.4	70.78	0.05739
Cr–O	12.69	3.701	0.9368	397.5	6.34	0.4343	392	0	0

[30] G. Wu, X. Zeng, G. Li, S. Yao, X. Wang, Mater. Lett. 60 (2006) 674.
[31] X. Zeng, G. Wu, S. Yao, Mater. Lett. 60 (2006) 2252.
[32] G. Wu, W. Dai, H. Zheng, A. Wang, Surf. Coat. Technol. 205 (2010) 2067.
[33] J. Yang, F. Cui, I.S. Lee, X. Wang, Surf. Coat. Technol. 205 (2010) S182.
[34] C. Wei, C. Gong, X. Tian, S. Yang, R.K. Fu, P.K. Chu, Plasma Sci. Technol. 11 (2009) 33.
[35] Y. Song, D. Shan, R. Chen, F. Zhang, E. Han, Surf. Coat. Technol. 203 (2009) 1107.
[36] C. Liu, Y. Xin, X. Tian, P.K. Chu, Thin Solid Films 516 (2007) 422.
[37] P. Fu, L. Peng, H. Jiang, J. Chang, C. Zhai, Mater. Sci. Eng., A 486 (2008) 183.
[38] J.F. Moulder, W.F. Stickle, P.E. Sobol, K.D. Bomben, J. Chastain, Handbook of X-ray Photoelectron Spectroscopy, Perkin-Elmer Corporation, Physical Electronics Division, Minnesota, United States of America, 1992.
[39] F. Guadarrama-Munoz, J. Mendoza-Flores, R. Duran-Romero, J. Genesca, Electrochim. Acta 51 (2006) 1820.
[40] G.M. Abady, N.H. Hilal, M.E. Rabiee, W.A. Badawy, Electrochim. Acta 55 (2010) 6651.
[41] Y. Xin, C. Liu, K. Huo, G. Tang, X. Tian, P.K. Chu, Surf. Coat. Technol. 203 (2009) 2554.
[42] Y. Xin, T. Hu, P.K. Chu, Corros. Sci. 53 (2011) 1522.